Estuary Plumes and Fronts in Shelf Waters: A Layer Model

RICHARD W. GARVINE

College of Marine Studies, University of Delaware, Newark, DE 19716

(Manuscript received 15 December 1986, in final form 5 April 1987)

ABSTRACT

A layer model that treats fronts as discontinuities is developed to study the steady state behavior of shallow estuary plumes on the continental shelf. The complete range of earth rotation effect is evaluated from small-scale or nonrotating plumes (Kelvin number equal zero) to large-scale, rotating plumes (Kelvin number equal order one). Supercritical flow is assumed in the outlet channel and the method of characteristics is used to compute the flow downstream. Nonrotating plumes have strong boundary fronts and concentrate their greatest layer depth and mass transport offshore near the front, but form no coastal current. Rotating plumes have boundary fronts that weaken soon after discharge, form a turning region where Coriolis action deflects the flow toward shore, and subsequently set up a coastal current. Soon after its formation this coastal current is bounded offshore by a strong front called the coastal front, across which the momentum balance changes from nearly inertial in the turning region upstream to nearly geostrophic in the coastal current itself. In traversing this front the flow loses total energy, but gains potential vorticity. Farther downstream the coastal front weakens, and meanders of the coastal current begin. Their wavelengths are short, about two Rossby radii, and their amplitudes grow, doubling after about 20 Rossby radii. The presence of supercritical speeds and fronts generates a plume dynamics that is remote from any linear description but shows analogous behavior to supersonic, compressible gas flow with shock waves.

1. Introduction

Estuary plumes, produced by the persistent discharge of brackish water, are primary mesoscale features of continental shelves and shelf seas. The larger-scale plumes react significantly to earth rotation. Boicourt (1973) presents surface salinity maps of the Chesapeake plume that show two principal flow regimes: a turning region where the plume, typically of depth 5 m, executes an anticyclonic turn beginning at the mouth and continuing until the isohalines approach the adjacent coast, and a coastal current of width roughly equal to the internal Rossby radius running parallel to shore with the coast on the right. Smaller-scale plumes lack clear evidence of Coriolis effects. The Connecticut River plume (Garvine 1974a) responds primarily to the alongshore tidal currents, reversing its deflection each tidal cycle almost symmetrically. Two length scales strongly influence estuary plume structure and dynamics: the length scale set by the geomorphology, principally the estuary width at the mouth, and the dynamical scale set by the internal Rossby radius. Their ratio forms a Kelvin number. Plumes with order-one Kelvin number may be expected to show strong Coriolis effects, such as the Chesapeake, while those with small Kelvin number should show weak effects, such as the Connecticut River.

Several model studies are relevant to estuary plumes with Kelvin numbers of order one. Takano (1954) published one of the earliest. His momentum balance included Coriolis acceleration, pressure gradient, and lateral friction. Contrary to Takano's claim that his results showed an anticyclonic turn for the current, however, Boicourt (1973) showed that Takano's solutions were symmetric about a straight line along the outflow initial direction. Nof (1978) developed an analytic model treating the steady, frictionless outflow of a shallow buoyant layer from a channel into a wide basin of unlimited length and containing deep, motionless, heavier water. The internal Froude number, the ratio of the discharge speed to the linear, long internal wave speed, was assumed small and used as the parameter in an asymptotic expansion. The model was not constrained to be quasi-geostrophic and retained nonlinear effects. Outflows with uniform velocity showed initial anticyclonic turning and, for higher Kelvin number, formation of a coastal current along the right-hand shoreline of the basin. No frontal structure was present. Beardsley and Hart (1978) also developed an analytic, steady state model. Both layers were active and simulated the action of the estuary on the adjacent shelf circulation by a point source discharge at the mouth for the upper layer and an equal strength sink for the lower layer. They neglected nonlinear effects, but retained both bottom and interfacial friction. They found that for the Northern Hemisphere the upper layer flow concentrated toward the left, contrary to most observations, while the bottom flow concentrated on the right. Their work thus implies that the tendency for the upper layer to turn right requires

the action of the inertial or nonlinear terms in the momentum balance. Chao and Boicourt (1986) applied a three-dimensional, primitive equation model to study the establishment of an estuary plume by discharge of fresh water into the upper reaches of a model estuary adjacent to an enclosed ocean basin. They used six layers in the vertical together with simple vertical diffusion and bottom drag. The horizontal grid size precluded resolution of fronts. Model experiments simulated conditions typical of Chesapeake Bay. Ten days of discharge were sufficient to establish a strong plume in the upper layer over the shelf having many of the observed features, including an anticyclonic turning region and a subsequent coastal current.

Garvine (1982) and O'Donnell (1986) developed layer models of the flow of a shallow, buoyant plume that included fronts as discontinuities where they applied appropriate jump conditions. Garvine (1982, hereafter called G82) treated the steady discharge of light water into an open domain of ambient water having uniform alongshore current. Earth rotation was neglected (Kelvin number zero). A strong front formed the offshore boundary of the plume. The results showed similar structure to the Connecticut River plume at slack tidal current. O'Donnell (1986) extended this model formulation to include time dependence and earth rotation. His results showed the complicated response of a plume discharged into a tidal regime for small Kelvin number. The frontal boundary, as for the steady state model of G82, was a dominant feature of both the plume structure and dynamics.

Observations of buoyant plumes nearly always reveal frontal structure, that is, the horizontal variation of plume properties such as density on a scale much smaller than the plume as a whole. A summary of some of these observations appears in an earlier paper (Garvine, 1981). Figure 1, showing a vertical density section across the Connecticut River plume, will serve here to illustrate frontal structure associated with a buoyant plume. The left-hand boundary of the plume labeled "surface front" has clear frontal structure in that horizontal density gradients there are much larger than elsewhere. For plumes, these fronts have a horizontal scale of the order 100 m (Garvine and Monk, 1974), and so are unaffected by Coriolis acceleration.

Since a variety of frontal forms will appear in the results of the present model, as well as in other models, I offer the following method for classifying small-scale oceanic fronts associated with buoyant surface layers. Two properties require classification: the relative location of a front and the degree of isopycnal (or layer depth) change there. I will use the term boundary front to denote one that forms all or part of the lateral boundary of a buoyant structure such as a plume, while I will use the term interior front for one having parts of the buoyant structure on each side. Thus, the front on the left of Fig. 1 is a boundary front, while the front labeled "coastal front" in Fig. 8 is an interior front. I

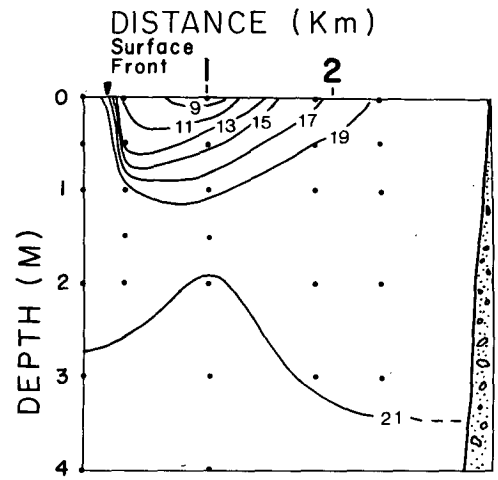

FIG. 1. Density (σ_t) section across the Connecticut River plume. The structure on the left marked "Surface Front" is a front of the depth discontinuity type, while the surface outcrop of the 19 isopycnal on the right is a front of the degenerate type. From Garvine (1977, Fig. 13).

will use the term depth-discontinuity type to denote fronts where buoyant layer isopycnals undergo finite depth changes across the front, or where the layer depth has finite change in layer models, while I will use the term degenerate type to denote fronts where this depth change is zero, as where the upper-layer depth vanishes smoothly. Thus, the front on the left of Fig. 1 is of depth-discontinuity type, while the front on the right formed by the intersection of the $\sigma_t = 19$ isopycnal with the free surface is of degenerate type. These two types present profoundly different structures for detection by observations. Observed horizontal density gradients will be much greater for the depth-discontinuity type than gradients in the buoyant layer itself, while gradients at the degenerate type will be of the same order as in the buoyant layer. The depth-discontinuity type will generate its own dynamic balance distinct from the buoyant layer dynamics (Garvine, 1974b; Kao et al., 1977), while the degenerate type will be mere free streamlines. Note that only boundary fronts can be degenerate types under the above definitions, because an interior front with the same layer depth on both sides would be no front at all.

To develop plume models that include fronts one must either resolve their structure properly or treat them as discontinuities. The former method requires the use of governing equations that are valid within as well as beyond the fronts. Kao et al. (1977) gave a clear example of this method for a nonrotating plume generated by a uniform line source of light fluid at a coast. The latter method requires use of suitable jump conditions that relate plume properties such as velocity on each side of a front; these conditions have close analogs in the Rankine–Hugoniot conditions for a shock wave in compressible gas flow and in the conditions for a hydraulic jump in open channel flow. In Garvine

(1981) I derived a set of such jump conditions for use with layer models. These accounted for conservation of mass and momentum in the direction locally normal to the front and, in particular, included the effects of mass entrainment, interfacial friction, and entrainment of momentum produced by exchange of mass and momentum between the buoyant and heavier layers. If the effects of this exchange are neglected, the jump relations simplify to the classical forms found for an internal hydraulic jump (Stoker, 1957, p. 318) provided the buoyant layer has finite depth on both sides of the front. Where the upper layer vanishes at a depth discontinuity type, however, as in the boundary front on the left in Fig. 1, the exchange effects must be included to obtain physically meaningful results. These jump relations, including the exchange effects, were subsequently employed in a series of buoyant layer models including G82, O'Donnell and Garvine (1983), Garvine (1984), and O'Donnell (1986).

Nof (1986) developed a model closely related to these but for application to rotating flow in a channel. His jump conditions were extensions of those used for hydraulic jumps in channel flow and similar to those applied to shock waves in a compressible gas flow. These neglected exchange of mass and momentum between layers for two-layer flows or exchange of momentum with the bottom (bottom friction) for single-layer flows; thus, they cannot be used to treat depth discontinuity types where the upper layer vanishes, as at the boundary front of Fig. 1, but will produce similar effects to those of Garvine (1981) when finite-layer depths exist on both sides. Nof explored the consequences of such a front when it acted as the transition in steady, rotating channel flow between two geostrophic, parallel flows, an upstream supercritical one and a downstream subcritical one. Most significantly, he found that such a front produced an increase in potential vorticity as the flow crossed it. Pratt (1983) found a small, but significant, increase across the front which formed in his numerical solutions of time-dependent flow over topography in a rotating channel and was able to derive jump relations for the increase. In this paper I find similar increases in potential vorticity as the plume water traverses an interior front. Such interior fronts thus may well serve to amplify potential vorticity in a variety of geophysical flows.

My major goal is to develop a layer model that includes fronts as discontinuities and that is applicable to steady state estuary plumes for the complete range of earth rotation effect from small-scale or nonrotating plumes with small or zero Kelvin number to large-scale, rotating plumes with order one Kelvin number. The model is essentially an extension of G82 to include earth rotation.

2. Governing equations

Figure 2 shows the essential model geometry. A shallow, upper layer of buoyant plume water flows from

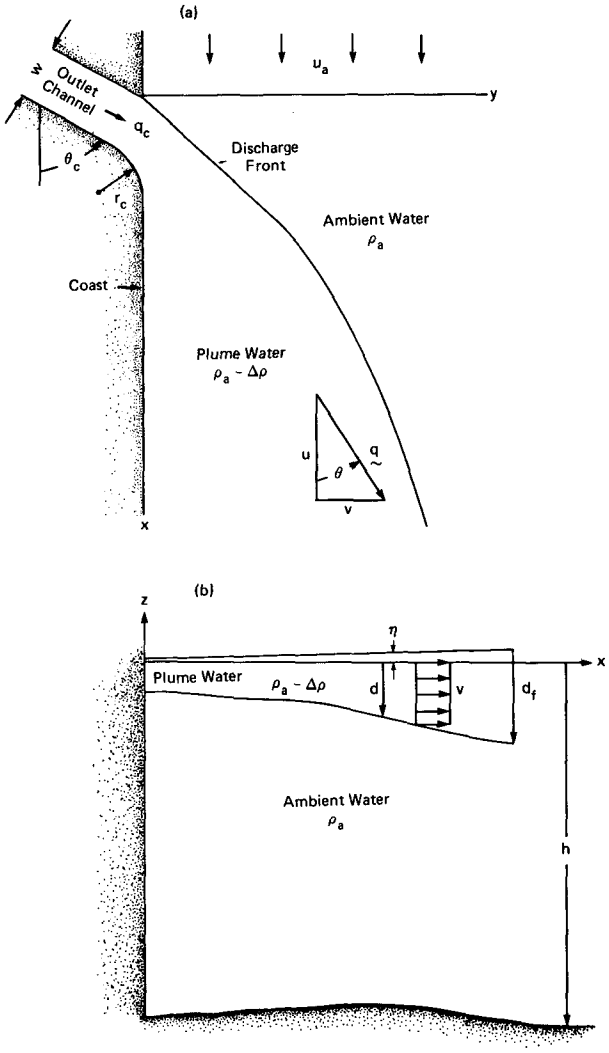

FIG. 2. Schematic of the model geometry. (a) Map showing the outlet channel and open coastal domain with ambient current u_a. (b) Vertical section through the plume.

an outlet channel of width w at the coast into an open domain at angle θ_c. The coastline is straight and coincident with the x-axis except at the righthand channel corner where it has a radius of r_c. Distance y is measured offshore from the lefthand channel corner and z is vertical, positive upward. The flow is steady in these coordinates with velocity $\mathbf{q}$ at angle θ to the x-axis and with horizontal components u and v. The plume depth d is small everywhere compared to total water depth h. The ambient water, representing inner-shelf water in most applications, has uniform density ρ_a and alongshore current u_a. For simplicity, the plume water is taken to have uniform density $\rho_a - \Delta\rho$ with $\Delta\rho/\rho_a \ll 1$, so that the Boussinesq approximation is valid. Because the plume is shallow, the pressure field is isostatic and free surface elevation is given by $\eta = (\Delta\rho/$

$\rho_a)d$; consequently, the horizontal pressure gradient in the upper layer is simply $\nabla p = \rho_a g' \nabla d$ where g' is the reduced gravity, $g\Delta\rho/\rho_a$. Wind stress is neglected, while interfacial friction, mixing, and mass entrainment between plume and ambient water are neglected everywhere but at fronts. Thus, except at fronts, the plume horizontal velocity $\mathbf{q}$ is vertically uniform. I treat fronts here as discontinuities whose structures are not resolved but across which I maintain mass and momentum balance through use of approximate jump conditions; these are simple extensions of those derived in Garvine (1981).

The continuity and horizontal momentum equations consistent with the above and applicable to the plume away from the fronts may be written in vector form as

$$\nabla \cdot (d\mathbf{q}) = 0, \tag{1}$$

$$(\mathbf{q} \cdot \nabla)\mathbf{q} + f\,\mathbf{k} \times \mathbf{q} + \nabla c^2 = 0, \tag{2}$$

where c is the long, linear internal wave phase speed given by $c^2 = g'd$, f the Coriolis parameter taken as constant, and $\mathbf{k}$ the vertical unit vector. These equations are the same as the shallow water equations used to describe the flow of a single layer of depth d under gravity and earth rotation (Gill, 1982) with g' here replacing g. They are strongly nonlinear for the present application because the Froude number $F \equiv |\mathbf{q}|/c$ will be of order one, in general.

I now introduce scaled variables for later convenience:

$$Q \equiv |\mathbf{q}|/c_0, \quad U \equiv u/c_0, \quad V \equiv v/c_0,$$

$$C \equiv c/c_0, \quad D \equiv d/d_0 = C^2,$$

$$X \equiv x/w, \quad Y \equiv y/w.$$

Here d_0 denotes the depth of the upper layer in the reservoir upstream of the outlet channel where it originates and $c_0 = (g'd_0)^{1/2}$, the reference phase speed. The only externally imposed horizontal length scale is w, the channel width. For nonrotating flow ($f = 0$), this is the only length scale, as in G82. Now, in contrast, the baroclinic Rossby radius $r_0 \equiv c_0/f$ becomes an intrinsic length scale for $f \neq 0$. The ratio of these two scales defines the principal parameter of the model, the Kelvin number

$$K \equiv w/r_0 \equiv fw/c_0.$$

Thus, nonrotating flows, as in G82, will correspond to the limit $K \to 0$, while earth rotation will be significant when $K = O(1)$.

Equation (1) permits use of a transport function $\tilde{\Psi}$ given by

$$\partial\tilde{\Psi}/\partial X = -DV, \quad \partial\tilde{\Psi}/\partial Y = DU.$$

Furthermore, the system (1)–(2) may be manipulated to show (Gill, 1982) that the Bernoulli function B (or mechanical energy) of the plume layer and the potential vorticity P are both conserved along streamlines, or lines of constant $\tilde{\Psi}$. In scaled variables, these statements may be written

$$B \equiv D + \frac{Q^2}{2} = B(\tilde{\Psi}), \tag{3}$$

$$P \equiv \left(\frac{\partial V}{\partial X} - \frac{\partial U}{\partial Y} + K\right) \Big/ D = P(\tilde{\Psi}). \tag{4a}$$

Equation (3) is simply Bernoulli's equation. For the special case when rotation is absent ($K \to 0$) and the outlet channel has uniform depth and speed, as in G82, $P = 0$ everywhere (irrotational flow) and $B = 1$ everywhere up to the boundary front. For $K > 0$, however, P and B will, in general, vary across streamlines. In addition, those streamlines that cross an interior front will suffer discontinuous changes there in P and B as a result of concentrated interfacial friction.

One may further manipulate (2), (3) and (4a) to find

$$P = -dB/d\tilde{\Psi}, \tag{4b}$$

valid for regions of frictionless flow. This convenient result is generally attributed to Charney (1955) in the geophysical literature, but has been much longer known in analogous form in compressible gas dynamics as Crocco's theorem (Crocco, 1937). It provides the most convenient expression for calculating P.

Following the evidence cited in G82, I will stipulate that the outlet channel flow is supercritical, that is, $F = Q/C > 1$ there. The method of solution I will use will then be based on the method of characteristics, as in G82, since the system (1)–(2) is then hyperbolic. Standard methods (Courant and Friedrichs, 1976) yield the three characteristic directions:

$$(dy/dx)_{\pm} = \tan(\theta \pm \phi), \tag{5a}$$

$$(dy/dx)_{\Psi} = \tan\theta. \tag{5b}$$

Here ϕ is the Froude angle, analogous to the Mach angle in supersonic compressible flow, given by

$$\phi = \sin^{-1}(F^{-1}) < 90°. \tag{5c}$$

Thus, the characteristic directions are given by the local streamline (5b) and a pair of lines (5a) inclined to either side of the local streamline at the Froude angle. The same methods also yield the following three independent ordinary differential equations that apply along a particular characteristic direction:

$$Qd\theta \pm \frac{2}{F\tan\theta}\,dC = -K\left[\cos\theta + \left(\frac{dy}{dx}\right)_{\pm}\sin\theta\right]dX, \tag{6a}$$

$$dQ = -\frac{2}{F}\,dC. \tag{6b}$$

Here (6a) is applied along the corresponding direction given by (5a) while (6b) applies along (5b). Thus, (6b) is merely Eq. (3), Bernoulli's equation, differentiated along a streamline. The characteristics form of (1)–(2)

for the three dependent variables C, Q and θ is then (3) and (6a), together with (5). The right-hand side of (6a), indexed by K, shows the action of Coriolis force on the flow. For $K \to 0$ with $P = 0$, (6b) is valid along any direction, corresponding to $B = 1$ in (3), and (6a) then reduces to Eq. (7) of G82.

I implemented this characteristic formulation using the first-order numerical finite-difference scheme described in G82. I began integration in the outlet channel and marched downstream. Typically, 100 grid points were used in the cross-stream direction. Provided the flow remains supercritical, the integration can be continued as far downstream as desired. Where critical flow ($F = 1$) was encountered at some point downstream, the solution domain was limited to points upstream. An independent estimate of the solution accuracy was provided by calculating P using (4b) in regions where the flow had not yet traversed a front and checking it against the original value in the outlet channel. Agreement was nearly always better than two percent.

3. Boundary conditions

At the solid boundaries given by the shoreline, including the outlet channel, the flow must parallel the boundary, since friction is neglected. This boundary condition is equivalent to specifying that the flow angle θ match that at the shoreline, $\theta_s(X)$.

At a point on the boundary front only two of the characteristic lines given by (5), $(dy/dx)_+$ and $(dy/dx)_\Psi$, connect the point with the known plume interior upstream. Thus, only (6b) and one of Eqs. (6a) are applicable, while four variables must be found at the front: C_f, Q_f and θ_f, as at interior points, and α, the angle of the front with the x-direction. The two additional constraints needed to close the system there are the two jump conditions, as used in G82, which represent the frontal-scale bulk conservation of mass and momentum locally normal to the front:

$$-Q_f \sin(\theta_f - \alpha) = S_e \beta U_a \sin\alpha, \tag{7a}$$

$$C_f = U_a \sin\alpha / F_a, \tag{7b}$$

where $U_a \equiv u_a/c_0$, the scaled alongshore current velocity, and

$$F_a = [2\beta(S_e + \tilde{d} - S_e^2\beta)]^{-1/2}, \tag{7c}$$

a Froude number for frontal propagation. Here S_e denotes the sign of the entrainment velocity, β the fractional extent of the frontal zone over which friction is important (Garvine, 1981), and $\tilde{d}$ is a parameter giving the relative strength of friction. Simpson (1982) reviews laboratory results on density currents which indicate that the best values for the parameters are $S_e = -1$ (downward entrainment or mass loss from the plume to the ambient water), $\beta = 0.15$, and $F_a = 1$, or from (7c), $\tilde{d} = 4.48$. Consequently, these are the values used here.

Where interior fronts developed, a more complicated set of jump conditions was required because the plume layer was present on both sides. I followed the scheme given in Garvine (1981), which accounts for mass continuity and momentum balance normal to the front, supplemented by a jump condition which accounts for momentum balance parallel to the front. I first found the layer depth D_d just downstream of the front (in the sense of the local flow) and local normal velocity $\bar{U}_d$ (positive toward the downstream side) from

$$D_d = [(a^2 + 4bD_u)^{1/2} - b]/2, \tag{8a}$$

$$\bar{U}_d = \bar{U}_u \frac{D_u}{D_d} + S_e\beta\left(1 - \frac{D_u}{D_d}\right)U_a \sin\alpha_i. \tag{8b}$$

Here α_i is the local angle of the interior front to the x-direction, $\bar{U}_u$ is the normal velocity just upstream of the front and D_u the depth there, and a and b are given by

$$a = D_u - (U_a \sin\alpha_i / F_a)^2$$

$$b = 2(\bar{U}_u - S_e\beta U_a \sin\alpha_i)^2.$$

Then I used the following jump condition to find the local parallel velocity just downstream of the front $\bar{V}_d$ in terms of that just upstream $\bar{V}_u$,

$$\bar{U}_d D_d(\bar{V}_d - U_a\cos\alpha_i) = \bar{U}_u D_u(\bar{V}_u - U_a\cos\alpha_i)$$

$$+ (S_e - \tilde{d})\frac{\beta}{2} U_a \sin\alpha_i (D_d - D_u)(\bar{V}_d - U_a\cos\alpha_i). \tag{8c}$$

This equation expresses the momentum balance locally parallel to the front as affected by interfacial friction and entrainment of momentum.

4. Outlet channel flow

The outlet flow state I used corresponded to the release of a thin, buoyant upper layer from an upstream reservoir, the upper estuary in applications, where the reduced gravity is g' and the depth d_0, or $D = 1$. The dimensional potential vorticity there is thus f/d_0, or $P = K$ from (4). The flow moves from the reservoir to the coast in the outlet channel wherein the flow is nearly parallel and in geostrophic balance with $P = K$ on all streamlines. Gill (1977) treated the single layer equivalent of this flow in detail, so I simply adapted his results. As Gill demonstrated, if the channel narrows sufficiently the flow will make a transition from a subcritical ($F < 1$) to a supercritical ($F > 1$) state in terms of across-channel averaged properties as at a control section for classical hydraulic channel flow. Subsequent channel widening downstream generates higher supercritical speeds, not a return to the upstream subcritical state. This corresponds to outlet channel layer depths D_c which decrease as the channel widens.

The primary parameter that defines the outlet channel flow is the transport parameter given by

$$\tau \equiv \frac{Tf}{2g'd_0^2},$$

where T is the dimensional upper-layer total volume transport. This parameter thus may also be written as

$$\tau = \frac{K}{2}\frac{T}{c_0 d_0 w},$$

and so is proportional to the Kelvin number and the scaled transport $T/(c_0 d_0 w)$. Consequently, for fixed transport $\tau \to 0$ as $K \to 0$, the nonrotating limit. For the Chesapeake plume τ is typically 0.2 and K about unity, while for the Connecticut River plume each is about a factor of ten smaller, reflecting the observed weakness of rotation.

The transport streamfunction clearly will depend on T. Hereafter I will use the convenient dimensionless form given by

$$\Psi = \frac{c_0 d_0 w}{T}\tilde{\Psi} = \frac{K}{2\tau}\tilde{\Psi},$$

with $\tilde{\Psi}$ as in section 2. Setting Ψ at zero at the right bank of the outlet channel (and, consequently, along the coast downstream) then dictates that $\Psi = 1$ along the left bank. For Southern Hemisphere applications ($f < 0$), one need only interchange right and left bank here.

The secondary parameter is Ψ_0, the value of Ψ in the interior of the reservoir, or equivalently, as Gill (1977) notes, the transport fraction exiting the reservoir along the right bank. The expression $\Psi_0 = 0$, for example, corresponds to exit on the left bank only, while $\Psi_0 = 1$ corresponds to exit on the right bank only. I will use $\Psi_0 = 1$, as observations tend to show lighter water concentrated on the right bank of the wider parts of estuaries such as Chesapeake Bay (Schubel et al., 1976).

For fixed τ and Ψ_0 Gill's (1977) Eq. (5.13) relates the channel width to $\hat{D}_c$, the average of the right and left bank layer depths in the channel, in the form of a quadratic equation. Selecting the appropriate branch here and using present variables, we have

$$t^2 = \frac{a - (a^2 - b^2)^{1/2}}{(1 - \hat{D}_c)^2}, \tag{9}$$

where

$$a \equiv 1 - \tau + 2\tau\Psi_0 - \hat{D}_c,$$

$$b \equiv \tau(1 - \hat{D}_c)/\hat{D}_c,$$

$$t \equiv \tanh\left(\frac{w_L}{2r_0}\right).$$

Here w_L represents the local unscaled channel width. For the present model I fixed $\hat{D}_c$ at 0.4 and then found w_L using (9). Since at the outlet $w_L = w$, (9) determines the Kelvin number, as $K \equiv w/r_0$. The above expression for t may be inverted to one for K using an identity for tanh:

$$K = \log\left(\frac{1+t}{1-t}\right).$$

Once the channel flow has become supercritical, continued widening of the channel will ultimately cause the layer depth at the left bank to vanish. For yet greater widths the flow separates from the left bank and is guided only by the right bank. Consequently, in the present model channel widths at the outlet greater than w_s, the width corresponding to separation, have no effect on either the outlet flow or the subsequent plume. Instead, the only effective length scale for the flow will be r_0. As Gill notes, separation first occurs when $\hat{D}_c = \tau^{1/2}$. Therefore, for given $\hat{D}_c$, the limiting, upper bound for τ is $\tau_s = \hat{D}_c^2$. Since I used $\hat{D}_c = 0.4$, the limiting value τ_s was 0.16 and the corresponding value for Kelvin number [using (9) with $\Psi_0 = 1$] was $K_s = 0.683$. The plume flow for greater τ is no different because the left bank at the outlet has no effect and could just as well be absent, the flow being totally right bounded. Thus, this limit may be used to describe the effect on a right-bounded coastal current of a turn in the coastline through the angle θ_c, the entire wedge of land shown in the upper left of Fig. 2a being absent.

With τ, Ψ_0, and $\hat{D}_c$ given and K computed from (9), the outlet channel flow state is now fully determined and given, following Gill (1977), by

$$D_c = 1 - \frac{(1-\hat{D}_c)}{\cosh(K/2)}\cosh[K(Y_c - 1/2)] - \frac{\tau}{\hat{D}_c}\frac{\sinh[K(Y_c - 1/2)]}{\sinh(K/2)}, \tag{10a}$$

$$Q_c = (1-\hat{D}_c)\frac{\sinh[K(Y_c - 1/2)]}{\cosh(K/2)} + \frac{\tau}{\hat{D}_c}\frac{\cosh[K(Y_c - 1/2)]}{\sinh(K/2)}, \tag{10b}$$

$$\theta = \theta_c, \tag{10c}$$

where Y_c is the scaled cross-channel distance ranging from zero at the right bank to one at the left. The associated scaled Bernoulli function, transport streamfunction, and potential vorticity are given by

$$B_c = D_c + \frac{Q_c^2}{2} = 1 + 2\tau(\Psi_0 - \Psi), \tag{10d}$$

$$\Psi_c = (D_{cR}^2 - D_c^2)/(4\tau), \tag{10e}$$

$$P_c = K. \tag{10f}$$

Because the channel flow is geostrophic, Ψ_c, given by (10e), is also the geostrophic transport with D_{cR} the layer depth at the right bank.

Figure 3 shows the outlet channel variables for what I will term the standard case: $\Psi_0 = 1$ and $\hat{D}_c = 0.4$, as

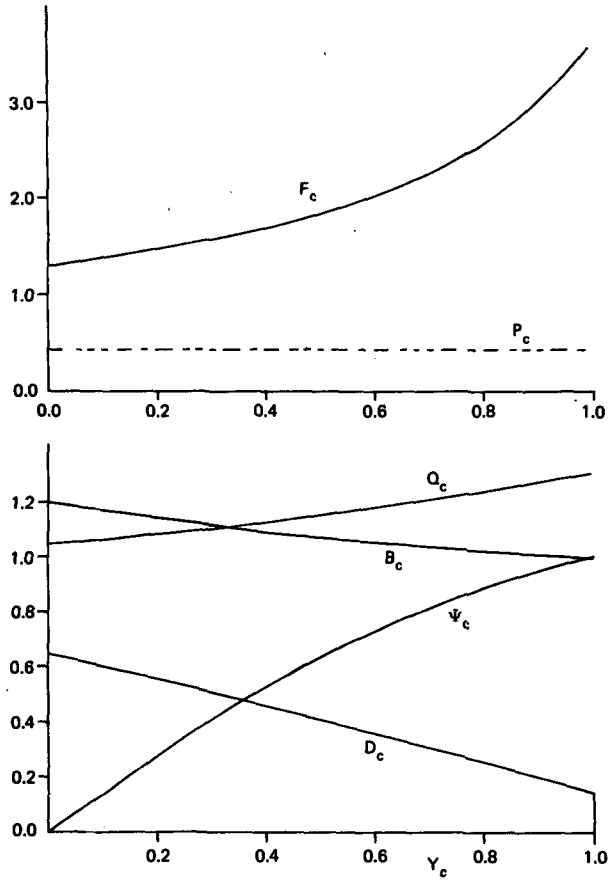

FIG. 3. Outlet channel flow state for the standard case. Y_c is the scaled distance across-channel from the right bank.

for all cases, and $\tau = 0.1$ corresponding to $K = 0.432$. The layer depth shows the flow "leaning" against the right bank (here shown on the left at $Y_c = 0$) with $D_{cR} = 0.65$ and thinning almost linearly with Y_c toward the left bank where $D = D_{cL} = 0.15$. The flow speed Q_c increases only slightly from 1.049 on the right bank. The Bernoulli function drops slowly across the channel from 1.2 to 1.0 with gradient in Ψ_c consistent with uniform $P_c = K = 0.432$. The Froude number $F_c = Q_c/D_c^{1/2}$ is supercritical with a lowest value of 1.30 on the right bank.

In addition to this local Froude number, another may be defined for this rotating channel flow where the relevant phase speed is that of a time dependent, small-amplitude, long wave rather than the local, long internal gravity wave speed. Gill (1977) gives such a Froude number in his Eq. (6.9). For the standard case its value is 1.88, or supercritical. Such organized long waves then also could not propagate upstream in the channel.

In contrast to the standard case, the nonrotating limit has an elementary flow state. Then, $\tau = 0 = K$, and $D_c = \hat{D}_c = 0.4$, $Q_c = 1.095$, $F_c = 1.732$, $B_c = 1$, and $P_c = 0$, while $\Psi_c = Y_c$.

As the flow exits the channel a discharge boundary front will form immediately at the left channel corner. For $D_{cL} > 0$, as for the standard case (Fig. 3), this front will be of the depth discontinuity type. Then, the jump conditions of (7a) and (7b) provide a link between channel angle θ_c and the ambient current U_a which ensures frontal properties consistent with steady flow. If we regard θ_c as given, then α_c, the initial frontal angle with the X-axis, and U_a are found by combining (7a) and (7b) to give

$$\alpha_c = \theta_c + \sin^{-1}\left(\frac{S_e \beta F_a}{F_{cL}}\right), \tag{11a}$$

$$U_a = F_a C_{cL}/\sin\alpha_c. \tag{11b}$$

The above implies that for $D_{cL} > 0$ the discharge front intersects the coast only at the left channel corner ($X = 0$, $Y = 0$), not, for example, at some point upstream ($X < 0$). Indeed, one may show that the intersection at the corner is the only possibility for a steady state. Time dependent flows would, however, remove this restriction.

For $D_{cL} = 0$ (separation) Eqs. (11) formally give $\alpha_c = \theta_c$ and $U_a = 0$. The discharge front then, however, is of the degenerate type, not the depth discontinuity type, so that no exchange of momentum or mass with the ambient flow there will occur; consequently, a steady state for this discharge front then imposes no constraint on U_a. (I outline the treatment of the degenerate type in the Appendix.) As noted above, the left channel bank need not even be present for this limit, and thus the question of where the front intersects the coast becomes moot, since the initial flow may be regarded as a coastal current directed along $\theta = \theta_c$, not necessarily as flow in a channel.

5. The nonrotating limit

The limiting case for $K \to 0$ is applicable to small-scale estuary plumes ($K = w/r_0 \ll 1$) or to flows lacking earth rotation. Such plumes were the main subject in G82; in this section I treat an example in order to provide contrasting structure to that for plumes with rotation.

Figure 4 shows a map of a plume for $K = 0$. Here, as for the standard case of section 6, $\theta_c = 40°$, the radius of curvature of the right bank corner is $R_c = 1$, and the frontal parameters are $S_e = -1$ (downward entrainment), $F_a = 1$, and $\beta = 0.15$. The ambient current speed is then $U_a = 1.114$, nearly the same as Q_c. The discharge front gradually turns toward the alongshore direction from its initial angle of $\alpha_c \approx 35°$. The paths of six streamlines are shown as dashed lines at uniform intervals of $\Delta\Psi = 1/7$. In the outlet channel these are distributed uniformly, because Q_c and D_c are constants, but beyond the mouth the outer three intersect the discharge front, a consequence of the downward entrainment there, while the inshore three are

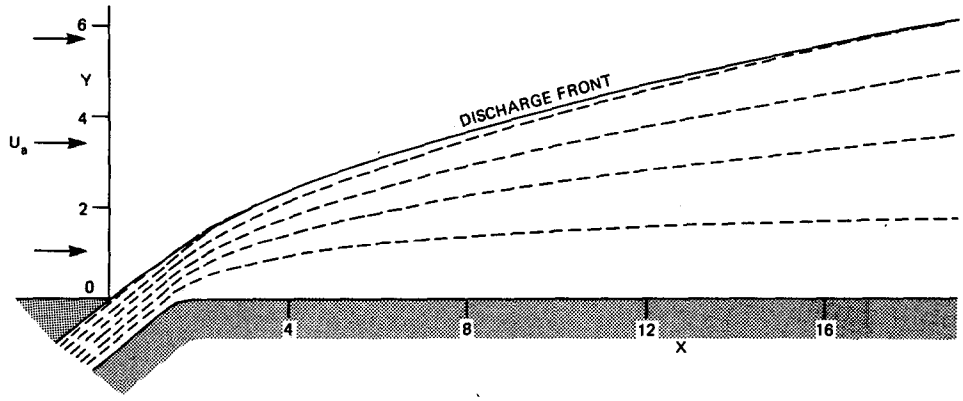

FIG. 4. Map of the plume for the nonrotating limit $K = 0 = \tau$ when $\theta_c = 40°$ and $R_c = 1$. Dashed lines show streamlines as lines of constant transport streamfunction at uniform intervals of $\Delta\Psi = 1/7$. Distances X and Y are scaled by outlet channel width w.

shifted offshore relative to their position in the channel. This shift toward the discharge front is a typical feature of nonrotating plumes. By $X = 20$ about $3/7$ of the total buoyant layer transport has been lost from the plume to downward entrainment at the discharge front to undergo subsequent mixing there with the ambient water, a testimony to the strength of the discharge front in nonrotating plumes.

Figure 5 shows an isometric projection of the layer-depth field $D(X, Y)$. The section at the far right shows a transect across the outlet channel passing through the left channel corner. Here the layer (or pycnocline) depth is greatest and uniform at $\hat{D}_c = 0.4$. Downstream the depth falls gradually as one would expect during gravitational spreading of a buoyant layer, but remains greatest at the front in any cross-shore transect. The plume is thus concentrated offshore, consistent with the offshore shift of streamlines shown in Fig. 4. As noted in G82, this feature is a direct consequence of nonrotating plume dynamics. The plume flow must adjust from its initial streamline angle of 40° to zero, i.e., it must turn right to become parallel to shore far downstream. Because both Coriolis force and interfacial friction are lacking, only cross-streamline pressure gradient can turn the flow. This, in turn, requires that the pressure or plume-free surface elevation η be greatest at the front. Consequently, because $\eta = (\Delta\rho/\rho_a)D$ from isostatic balance in the vertical, D also must be greatest there.

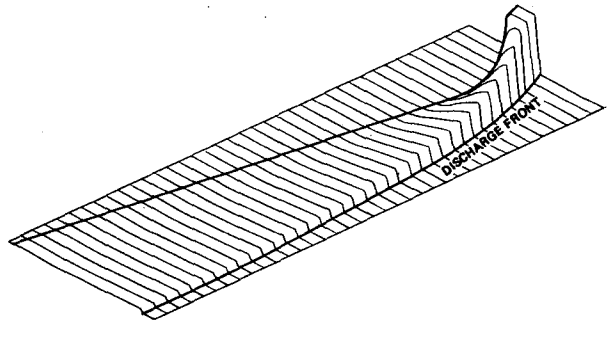

FIG. 5. Isometric view of layer depth D plotted upward for $0 < X < 8$ of nonrotating plume shown in Fig. 4. The right-most transect passes through the left-hand channel corner.

Hallmarks of nonrotating plume structure, then, are the strength of their discharge fronts with attendant mass flux loss there to entrainment and the concentration of the plume offshore toward the front with the deepest pycnocline there along any cross-shore section. The only length scale is that imposed by the channel width.

6. The standard case

Figure 6 shows a map of the plume for the standard case with $\tau = 0.1$ ($K = 0.432$), $U_a = 0.637$, and the same channel and shoreline geometry as for the nonrotating plume of Fig. 4. (The same map will serve for Southern Hemisphere applications, $K < 0$, if the plot is simply inverted in X about the Y-axis.) Significant differences from the nonrotating plume are clear. While the discharge front and streamlines begin turning anticyclonically (to the right in the Northern Hemisphere), as for the nonrotating plume, they continue to turn and, unlike the nonrotating plume, all begin to approach the coast ($\theta < 0$). This turning region, as I will show subsequently, is one of nearly inertial balance with little horizontal pressure gradient acting, in sharp contrast to the nonrotating dynamics. The trajectories, including that of the discharge front, closely approximate the arcs of inertia circles, the outer streamlines having greater radii of curvature as a consequence of the greater flow speed there. This turning region has been identified in field observations of the Chesapeake plume (Boicourt, 1973) and appears in clear form as well in the fully three-dimensional numerical model results of Chao and Boicourt (1986).

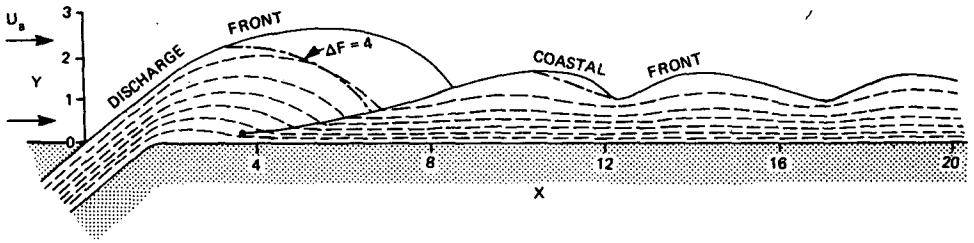

FIG. 6. Plume map for the standard case. Dash–dot line indicates where $\Delta F = 4$, solid circle where coastal front is first fitted computationally.

As the plume water approaches the shore after the turn, it encounters the locally high pressure near shore needed to force it to turn cyclonically (left) toward parallel to shore. Again, because of the isostatic nature of the pressure field, high pressure (or high η) coincides with greater D, and thus the relatively deep shore-parallel flow begins to form on the right of the plume. At first this turning occurs gradually, but as more plume water approaches shore an interior front forms of the depth discontinuity type.

Details of the interior front formation are best seen in Fig. 7 for a similar plume (but with $K = 0.627$). There not only the streamlines but also the two families of characteristic lines or wavefront envelopes appear, the latter traced using Eq. (5a) from a selected point on each streamline near the mouth. The left-running characteristics merely coalesce with the discharge front after it becomes weak, but the initially right-running ones approach and reflect off the shore as waves of the left-running family. Note how several of these coalesce just offshore near $X = 3$. Superposition of characteristics of the same family leads to formation of a discontinuity (Courant and Friedrichs, 1976), in this flow an interior front which I call the coastal front, as it serves to bound the developing coastal current inshore. The solid circle in Fig. 7 shows where jump conditions were first used to represent the discontinuity. Downstream from there the front strengthens as more plume water sweeps across it into the progressively deeper and wider coastal current. Now streamlines change direction discontinuously at the front from onshore to nearly shore-parallel. Left-running characteristics are trapped in the coastal current, unable to escape the front seaward because of the high-speed, onshore-moving flow there.

The coastal front grows in the same way for the standard case (Fig. 6). As more of the total plume volume flux builds behind it in the coastal current, the front

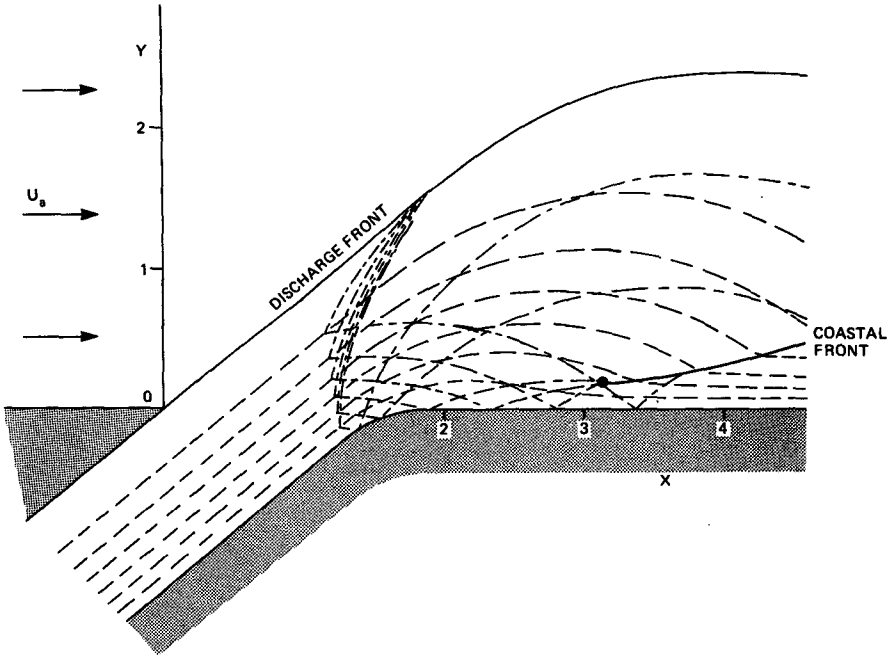

FIG. 7. Map of plume showing details of coastal current and coastal front formation. Same conditions as standard case of Fig. 6, except $K = 0.627$. Dashed lines are streamlines, dash–dot lines are characteristic lines radiating from a selected point on each streamline.

migrates seaward, intersecting the now degenerate discharge front at about $X = 8$. Subsequently, it becomes the boundary front and continues as a depth-discontinuity type until about $X = 10$ where it too becomes degenerate, a mere free streamline. At about this distance still another plume property emerges that was lacking in the nonrotating case. Wavelike meanders of the coastal current appear with apparent wavelengths of about $\Delta X = 4.7$ (or, multiplying by $K = w/r_0$, about 2.0 Rossby radii) and amplitudes of about $\Delta Y = 0.35$. The mean current width is about 1.3 or 0.56 Rossby radii. Both the front and all streamlines oscillate in phase, so that only a "lowest mode" behavior is evident. As I will show later, these oscillations grow slowly downstream and the coastal current becomes unstable.

While the model results formally predict the weakening of depth discontinuity fronts to form degenerate types, in nature vertical shear flow instability would intervene before degeneracy could happen. Near degenerate fronts the fluid speed in the plume remains finite while the layer depth vanishes so that the vertical shear grows without limit. To estimate where vertical shear instability would first occur along a trajectory in the plume I computed the bulk shear Froude number $\Delta F \equiv |(U - U_a)\mathbf{i} + V\mathbf{j}|/C$, i.e., the local bulk shear velocity between plume and ambient water divided by the local phase speed. Thus, ΔF is the inverse square root of the corresponding local bulk Richardson number. While stable flow is guaranteed for $\Delta F < 2$, corresponding to Richardson number $> \frac{1}{4}$, sufficiently large ΔF will trigger instability, usually in the form of Kelvin-Helmholtz billows. I chose $\Delta F = 4$ as an indicator of the locus for instability and local, rapid vertical mixing based on O'Donnell's (1986) results. Along streamlines downstream of this locus one would expect the plume to disappear in nature, even though the model may still show plume structure.

The dash-dot line in Fig. 6 shows the locus for $\Delta F = 4$. It indicates that the plume in the triangular region bounded by the discharge front, the coastal front, and the locus would suffer vertical mixing and likely be unobservable there. Most of the original streamlines avoid this region, however, and reach the coastal current. Inside the coastal current the flow remains stable vertically because it is slower and much deeper, until further downstream near $X = 10$ where the coastal front itself approaches the degenerate type. Then the outermost parts of the coastal current likewise would suffer instability. Thus, despite their occurrence in the model, degenerate plume fronts are not likely to exist in nature.

Figure 8 shows a projection of the layer depth field for the standard case downstream to $X = 8$. It presents a strong contrast to the nonrotating structure of Fig. 5. In the exit channel the buoyant layer clearly "leans" against the right-hand channel until it reaches the corner. The discharge front initially has modest strength ($D_f = 0.15$) but its decline to degeneracy is swift leading to its near invisibility downstream of where it is drawn.

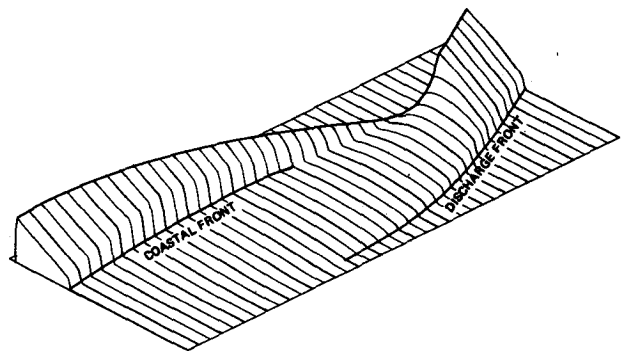

FIG. 8. Isometric view of layer depth D for $0 < X \leq 8$ for the standard case (Fig. 6).

In this figure the turning region appears as a broad, shallow plateau where only feeble depth gradients, and hence pressure gradients, prevail, unlike Fig. 5. Near the right channel corner D falls shoreward, as in the nonrotating plume, assisting the flow in its sharp turn there. The coastal current arises soon after, deepens, spreads, and then acquires its coastal front boundary. The front gains strength as a depth discontinuity front, then begins to weaken as the coastal current roughly acquires the structure of the outlet flow. As shown below, the flow here is nearly geostrophic again.

Figures 9 and 10 show transects of the major plume properties along two cross-shore sections. At $X = 4$ the transect of D shows four primary features: the discharge front in a state of great weakness, the shallow plateau of the turning region, the coastal front with moderate strength, and the nearly geostrophic coastal current. Near the discharge front ΔF exceeds 4, but elsewhere the flow should be vertically stable, especially in the coastal current where ΔF falls to about unity. The flow speed drops abruptly as the flow crosses the coastal front because of intense friction there. Note the corresponding drop in total energy B behind the coastal front, a result of the frictional dissipation of energy there or "head loss" in hydraulic terms. At the coast, however, $B = 1.2$ still, as along the right bank of the outlet channel, since the streamline passing along the shore never traverses the coastal front. Consequently, within the coastal current B drops seaward more rapidly than it would have without frontal dissipation. This drop, in turn, generates higher potential vorticity $P = -(K/2\tau)dB/d\Psi$, peaking at about $P = 2$ here behind the front. These elevated values contrast with the original value $P = K = 0.432$ of the outlet channel. Nof (1986) likewise found that the interior front that developed in his steady rotating channel flow produced significant increase in P, while Pratt (1983) found a small, but significant, increase for time dependent rotating channel flow crossing a similar front. In the turning region beyond the coastal front P is conserved and thus $P = K$ there still. Thus, the coastal front itself by its dissipation of energy produces both enhanced

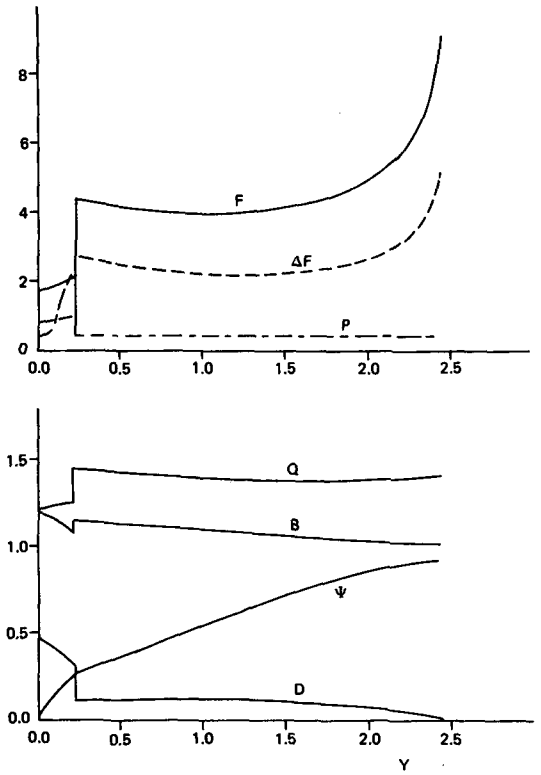

FIG. 9. Plume properties vs Y for the standard case at $X = 4$. The discharge front is near $Y = 2.4$ while the coastal front is near $Y = 0.2$.

potential vorticity and a potential vorticity gradient within the coastal current. In this way the flow state of the coastal current differs markedly from that in the outlet channel, despite the common geostrophic and layer depth structure. Most linear stability analyses of nearly geostrophic currents show cross-stream gradients in potential vorticity as the key stability determinant.

Figure 10 shows another transect, this one well downstream at the meander crest at $X = 14.3$. The coastal front itself has become degenerate but just behind it the flow would be vertically unstable as ΔF rises steeply there. Elsewhere ΔF is about unity. After passage through the upstream coastal front, the various streamlines now in the coastal current have conserved the values of B and P they acquired then. Note the strong decline now in B from 1.2 at the coast to only about 0.4 behind the present front, consistent with the decreased Q there. The strong gradient in B produces a strong gradient in P with a peak value of about 9 near the front, about 20 times the initial, uniform value K upstream. Consistent with heightened P is the change in sign and increase in magnitude of the relative vorticity, now roughly equal to $-\partial U/\partial Y \approx -\partial Q/\partial Y > 0$. Unlike the cross-channel transect (Fig. 3) $\Psi = 0.86 < 1$ now at its outer edge, reflecting modest upstream mass flux losses at both the discharge and coastal fronts to downward entrainment.

Figure 11 shows layer depth contours together with the value of terms in the across-stream momentum balance for $X \leq 8$. The layer depth contours in Fig. 11a provide a companion view to the isometric projection of Fig. 8. Note that the peak values of D at the coast, about 0.65, are the same as at the right bank in the outlet channel.

The momentum balance of Eq. (2) may be rewritten in terms of local streamline coordinates. With S the scaled distance along a streamline (positive downstream) and N the same across it (positive leftward) we have

$$Q^2\frac{\partial\theta}{\partial S}+KQ+\frac{\partial D}{\partial N}=0, \tag{12a}$$

$$Q\frac{\partial Q}{\partial S}+\frac{\partial D}{\partial S}=0. \tag{12b}$$

Equation (12b), the streamwise momentum equation, is merely the equivalent of (3), Bernoulli's equation, and necessarily lacks the Coriolis term. However, (12a), the across-stream momentum balance, provides a compact assessment of the local competition between the relative acceleration $Q^2\partial\theta/\partial S$, resulting from local streamline curvature, Coriolis acceleration KQ, and

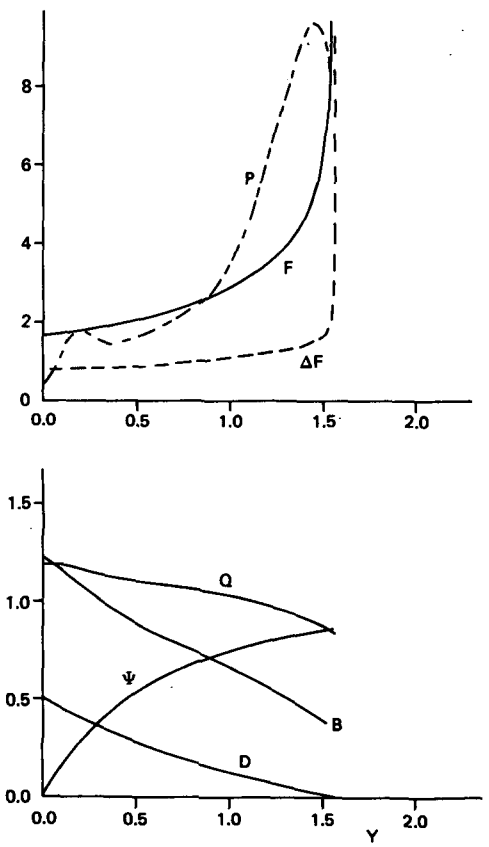

FIG. 10. As in Fig. 9, but at $X = 14.3$, the location of a coastal current meander crest.

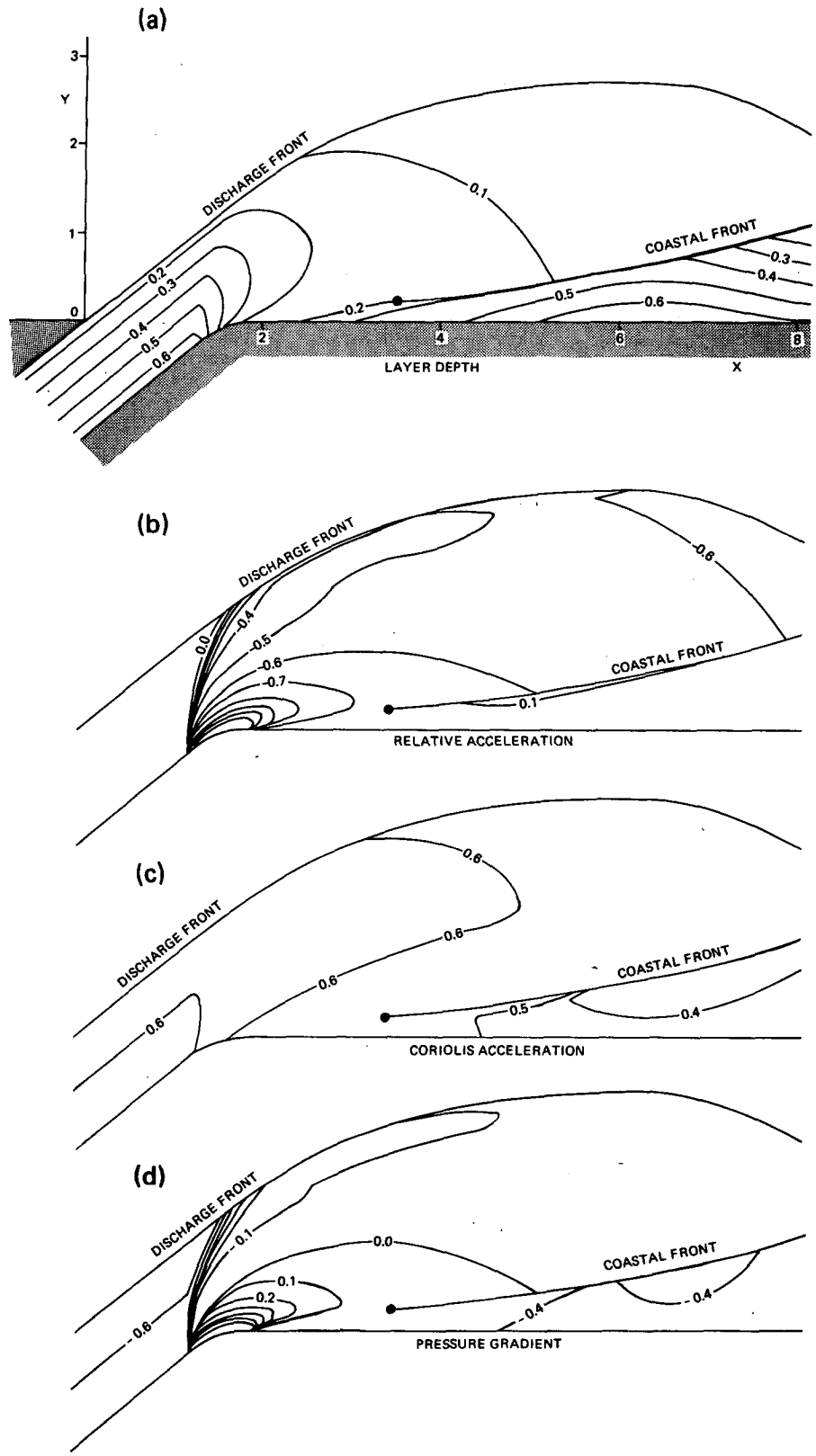

FIG. 11. Contour lines for layer depth and across-streamline momentum balance terms of Eq. (12a) for the standard case; (a) layer depth, (b) relative acceleration $Q^2\partial\theta/\partial S$, (c) Coriolis acceleration KQ, (d) pressure gradient $\partial D/\partial N$.

across-stream pressure gradient $\partial D/\partial N$. For nonrotating flow $K = 0$ and (12a) reduces to a balance between relative acceleration and pressure gradient. Then, as Fig. 5 showed, the plume will always deepen offshore in cross-shore transects to balance the relative acceleration. Two other simple (two-term) balances are possible: inertial turning, when relative and Coriolis accelerations balance in the absence of pressure gradient, and geostrophic balance, when relative acceleration is absent.

Figures 11b, c and d show maps of the terms in (12a) in the order written. In the outlet channel the flow is specified as geostrophic and the three maps merely reflect this balance. Immediately as the flow reaches the beginning of the right channel corner strong wave fronts radiate along left-running characteristic lines producing a rapid increase (algebraically) in pressure gradient and corresponding negative relative acceleration with little change in Coriolis acceleration. The initial adjustment to flow expansion is essentially irrotational, because Coriolis effects require significant particle displacement to affect change. Near the curving shoreline locally large relative accelerations build, balanced in part by the pressure gradient generated by the layer depth dipping toward shore. Beyond here the flow quickly enters the turning region where the layer depth thins and becomes nearly uniform at about $D = 0.1$ (Fig. 11a). The pressure gradient vanishes along the middle of this region and, as Figs. 11b and c show, near inertial balance is achieved with each term about 0.6 in magnitude. This balance nearly holds now throughout the entire region offshore of the coastal front and inshore of the discharge front. Nonetheless, as the flow crosses the coastal front the momentum balance switches again, this time discontinuously, to near geostrophic balance in the coastal current. Only in the formation region is there significant relative acceleration in the current, just those positive values associated with the gradual cyclonic turn there. Further downstream the flow turns discontinuously in the coastal front instead (Fig. 6). Finally, in the meander region (not shown) the relative acceleration once again becomes moderate, up to 20% of the Coriolis acceleration.

Over the bulk of the plume, then, the momentum balance for $K = O(1)$ is either nearly geostrophic, in the outlet channel and coastal current, or nearly inertial, in the turning region. The transition regions between are small. Such rapid switching is remote from any linear behavior; indeed, the momentum balance itself involves the nonlinear relative acceleration term in the turning region. Such strong nonlinearity is a direct consequence of the supercritical flow speeds in the plume. The complexity of the flow compared to the nonrotating limit is a consequence of the action of a second length scale, the Rossby radius r_0.

The present results show strong similarity to the numerical model results of Chao and Boicourt (1986), especially for their first experiment where vertical mixing was limited. Ten days after flow initiation their uppermost layer showed a distinct anticyclonic turning region that they termed the "bulge," followed downstream by a sharp transition region of cyclonic turning into a coastal current. Their model did not include fronts as discontinuities nor could fronts be resolved by the coarse computational grid, but the sharp transition region they found closely resembles the coastal front of the present model where it is of the depth discontinuity type. The vertical velocity fields at the bottom of the buoyant layer of the two models are also highly similar. Here the vertical velocity at the pycnocline (scaled by $c_0 d_0/w$) may be written as $W = -Q\partial D/\partial S$. Since $Q > 0$, W here always has the opposite sign of $\partial D/\partial S$. Thus, $W = 0$ in the outlet channel, becomes strongly positive (upwelling) where the plume turning is initiated (Fig. 11a), then weak in the inertial turning region, and finally nearly zero in the coastal current where near geostrophy is reached. At both the discharge and coastal fronts intense sinking occurs, consistent with the downward entrainment active there, except where they have become degenerate. Especially if one interprets the field of vertical velocity Chao and Boicourt present as including regions where fronts are smeared out, the qualitative agreement in vertical velocity is strong.

7. Other cases

Once the outlet channel state reaches separation from the left bank ($D_{cL} = 0$), only one plume length scale exists, the Rossby radius r_0. As noted in section 4, this occurs when $\tau_s = \hat{D}_c^2 = 0.16$ ($K_s = 0.683$). Figure 12 presents the plume map for separation when the channel angle is $\theta_c = 30°$ and Fig. 13 is the corresponding layer depth field. While the left bank appears in Fig. 12, it has no effect on the plume. Its removal leaves a map showing the consequences of the turn of a coastal current with uniform P imposed by a bend in the coast of 30°. At first U_a has no effect either, because the discharge front is degenerate so that no coupling between the plume and ambient flow exists for the entire region beyond the coastal front. I was thus free in that respect to select a value and chose $U_a = 1$.

The flow pattern for this limiting case is qualitatively similar to the standard case. The degeneracy of the discharge front is clear in the isometric view of Fig. 13. Note the presence in Fig. 12 of the line marking where $\Delta F = 4$ just inshore of the front and outlining a more likely offshore edge for the plume in nature. Because the front has zero strength, $D_f = 0$, it lacks entrainment power; consequently, streamlines run parallel to it and no plume mass is lost there. The turning region, coastal current, and downstream meanders are all qualitatively the same as for the standard case. The mean coastal current width is $Y = 1.1$ or 0.75 Rossby radii. The meanders likewise become unstable well downstream. Their properties are summarized in this section.

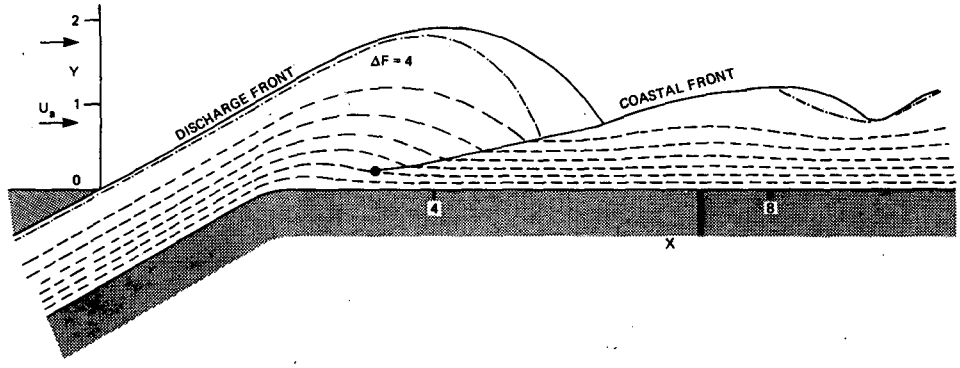

FIG. 12. Plume map for the limiting case of separated flow at the left bank of the outlet channel when $\tau = 0.16$, $K = 0.683$ and $\theta_c = 30°$ with $U_a = 1$.

The particular value of U_a selected has a modest effect on the coastal front upstream of its junction with the discharge front and a crucial effect on it downstream where it becomes a boundary front of the depth discontinuity type whose behavior is governed by (7). Such fronts must propagate or spread *relative* to the ambient current in the direction locally normal to the front. Thus, to remain stationary in space, as required in this steady state model, the ambient current must have a local normal component *toward* the front, or $U_a \sin\alpha_{cF} > 0$, where α_{cF} is the angle of the coastal front. Here $\sin\alpha_{cF} > 0$ everywhere downstream until the front becomes degenerate (roughly where the $\Delta F = 4$ line intersects it in Fig. 12). Once the coastal front is degenerate, the value of U_a is immaterial again, but before that the frontal dynamics requires $U_a > 0$ for a steady state to exist.

Guided by these properties of a steady state plume with separated channel flow, we may anticipate the time-dependent response for a case when the ambient current changes sign following a steady period during which $U_a > 0$. Such a current change on the inner shelf could result, for example, from a change in direction of the alongshore wind toward negative X. The model results indicate that the turning region and meander region would not be much affected, but in the region between them where the coastal front is a nondegenerate boundary front, we may expect the front to turn left and propagate offshore and toward negative X so as to overtake the current and maintain a flow of ambient water relative to it still. The plume layer behind it would be forced by pressure gradient to follow, thinning in the process. O'Donnell's (1986) numerical results for such a time-dependent plume with a small Kelvin number show similar qualitative features.

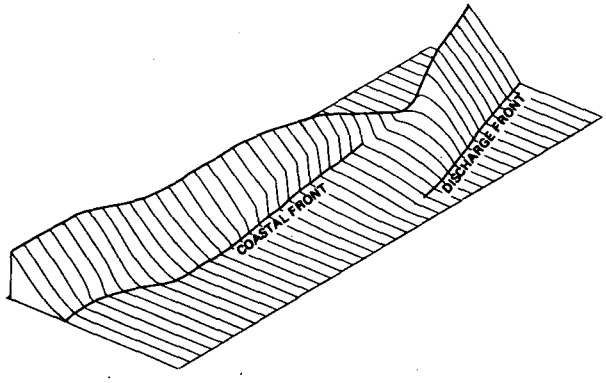

FIG. 13. Isometric view of layer depth D for $0 < X < 10$ for plume shown in Fig. 12.

The results presented thus far have been for channel angles $\theta_c \leqq 40°$. Figures 14 and 15 show plume maps for $\theta_c = 90°$ and $R_c = 0.05$, i.e., for outflow perpendicular to the coast and a sharp right-hand channel corner. In Fig. 14 the outlet channel flow is again in the nonrotating limit $\tau = 0 = K$ and, except for $\theta_c = 90°$ and $U_a = 0.635$, is identical to that of Fig. 4 where $\theta_c = 40°$. In Fig. 15 I use the same channel geometry but small, nonzero Kelvin number with $\tau = 0.02$ or $K = 0.09$ and $U_a = 0.593$.

When compared to Fig. 4, the main feature of the nonrotating plume of Fig. 14 is the additional rotation of the plume by about 50°. More careful examination, however, shows two new physical properties.

First, the right bank streamline separates from the shore before it can complete the 90° turn following discharge. As noted in G82, the maximum angle through which such a streamline may be turned upon discharge is about 66° for nonrotating flow; greater channel angles θ_c cause surfacing of the plume inshore along a straight line. In Fig. 14 this streamline is labeled "$D = 0$". It is, of course, also a degenerate front. Once again, however, local vertical mixing would obliterate it. The line is straight because Coriolis effects are absent. Along it plume water reaches its highest speed, $Q_{max} = [2(B - D)]^{1/2} = 2^{1/2}$, since $B = 1$ everywhere.

Second, the plume takes on a "ring" structure downstream. Note the geometry of the characteristic lines illustrated as in Fig. 7. Now those that are initially right-running cannot reflect off the coast, as there is no plume water there, but merely diverge slowly while trending in the general flow direction on the shallow,

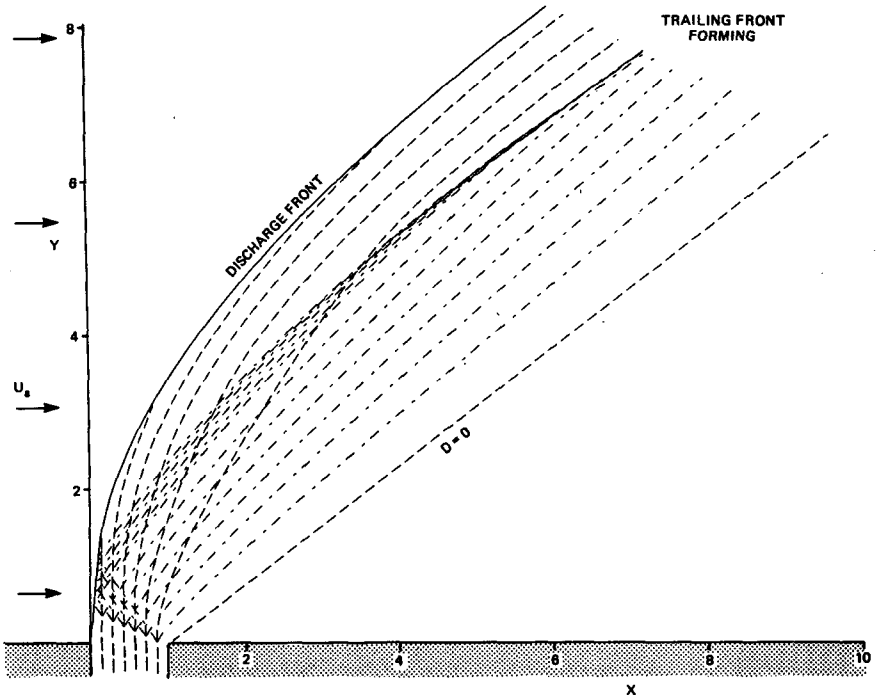

FIG. 14. Plume map for the nonrotating limit $K = 0 = \tau$ when $\theta_c = 90°$ and $R_c = 1$. Compare to Fig. 4. Characteristic lines as in Fig. 7. Line labeled $D = 0$ marks streamline or degenerate front that separates from shore at right channel corner.

inshore side of the plume. The initially left-running characteristics, however, reflect off the strong discharge front and travel downstream as a converging beam. They coalesce at about $X = 7$ to form a trailing front. Between this front and the discharge front nearly all the mass flux that has escaped loss to frontal zone entrainment is concentrated, giving the layer depth there a roughly "top hat" shape locally and a ring shape globally. Such ring structure is ubiquitous for the nonrotating, radially symmetric discharge of buoyant fluid in time-dependent flows (Garvine, 1984) and occurs frequently in O'Donnell's (1986) results for two-dimensional, time-dependent plumes at small or zero Kelvin number.

The results shown in Fig. 15 show the striking effects of adding a small amount of rotation (small Kelvin number) to the flow of Fig. 14, or, put differently, of adding a second length scale, the Rossby radius. Near the mouth the flow is quite similar, since Coriolis effects require finite time or particle displacement to act, but by about $X = 11$ (about $0.6r_0$ downstream) significant differences are clear. No ring is forming; instead, all streamlines, including the inshore one where $D = 0$, are turning right under Coriolis action. The plume reattaches to the coast at about $X = 19$ ($1.7r_0$) after which the remaining streamlines come ashore to form a coastal current. The discharge front weakens to a degenerate front and turns shoreward, as well. All the major plume subregions present for $K = O(1)$ (Figs. 6 and 12) recur: the inertial turning region, the coastal front, the coastal current, the meander region, and the downstream instability; only the scale in X (channel

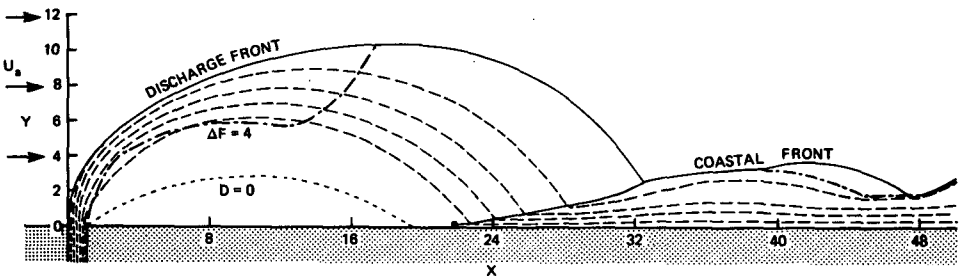

FIG. 15. Plume map for small rotation, $\tau = 0.02$, $K = 0.09$ with $\theta_c = 90°$ and $R_c = 0.05$.

widths) is different. However, the scale in terms of Rossby radius is similar. The discharge and coastal current fronts intersect, for example, at $x/r_0 \approx 3$ for the present case ($K = 0.09$) and at $x/r_0 \approx 3.7$ for the standard case ($K = 0.432$). The mean coastal current width is 2.7 or 0.25 Rossby radii.

While the similarity in structure for quite different K is simplifying, an essential difference remains. In Fig. 6 the great bulk of the plume is turned back to the coast and enters the coastal current without ΔF exceeding 4, but in Fig. 15 nearly all the flow reaches $\Delta F > 4$ in the turning region and so is unlikely to survive vertical mixing before entering a coastal current where $\Delta F \approx 1$.

Discharges with $\theta_c = 90°$, $\Psi_0 = 1$, and $\hat{D}_c = 0.4$, but with $\tau > 0.02$ ($K > 0.09$) develop subcritical flow ($F < 1$) in their coastal currents downstream. Consequently, the method of characteristics fails there and a different solution method would be needed to compute the flow state downstream of the critical point. Such flows are fundamentally, not just computationally, different because long internal wave disturbances then may travel upstream as well as downstream in the coastal current. Consequently, perturbations may propagate upstream from some disturbance downstream, such as an outward bend in the coastline, and be felt upstream everywhere that $F < 1$. The steady flow problem then becomes a split boundary value problem in x, not simply a downstream marching problem from a given flow state near $x = 0$.

I investigated the conditions under which subcritical flow developed downstream by using outlet channel states with $\Psi_0 = 1$, $\hat{D}_c = 0.4$, and $R_c = 0.05$, as above, and increasing θ_c for fixed τ (or K). Figure 16 shows the results in the parameter space θ_c vs τ. Below and to the left of the solid curve flows were supercritical everywhere, including in the coastal current. Above and to the right of the dashed line all flows reached subcritical speed somewhere downstream in the coastal current. The separation of the two lines, about 2.5° in θ_c, represents the increment used in θ_c for successive integrations at fixed τ. For sufficiently small $\tau < 0.02$ or $K < 0.09$ (as in Figs. 14 and 15), completely supercritical flows result for all angles $0 < \theta_c \leqslant 90°$, while for $\theta_c < 30°$ the same is true for all τ. The maximum θ_c permitted at fixed τ for uniformly supercritical flow reaches the minimum level of about 30° at $\tau \approx 0.14$, then increases slightly at $\tau = 0.16$, the limiting or separation value. The model results thus indicate that for larger-scale plumes ($K = O(1)$) subcritical coastal currents will often be present permitting upstream influence, while for small-scale plumes ($\tau < 0.02$ or $K \ll 1$), only uniformly supercritical coastal currents exist. For nonrotating plumes ($\tau = 0 = K$) no coastal current develops and the plumes are necessarily supercritical everywhere.

I carried the computation of three cases with supercritical coastal currents far downstream to quantify their unstable meander growth: the case for $\tau = 0.02$ of Fig. 15, for $\tau = 0.10$ (the standard case) of Fig. 6, and for $\tau = \tau_s = 0.16$ (separation) of Fig. 12. Figure 17 shows the growing meanders for the standard case; the other two cases are qualitatively the same. The first four streamlines beyond the coast ($\Psi = 1/7, 2/7, 3/7$ and $4/7$) are plotted from $X = 10$ to 100 (x/r_0 from 4.3 to 43). The streamlines oscillate in phase, as in a first-mode wave, and maintain a nearly constant wavelength of $\lambda = 4.7w$. The meanders are thus not long waves, since the total mean current width (about $Y = 1.3$ from Fig. 6) to wavelength ratio is about 0.28. The meander amplitude grows slowly, doubling after a distance $x_2 = 48w$ or 20.7 Rossby radii. Table 1 summarizes properties of the meanders for the three cases. Both λ/r_0 and x_2/r_0 increase with τ reaching 2.3 and 25.4, respectively, for $\tau = 0.16$.

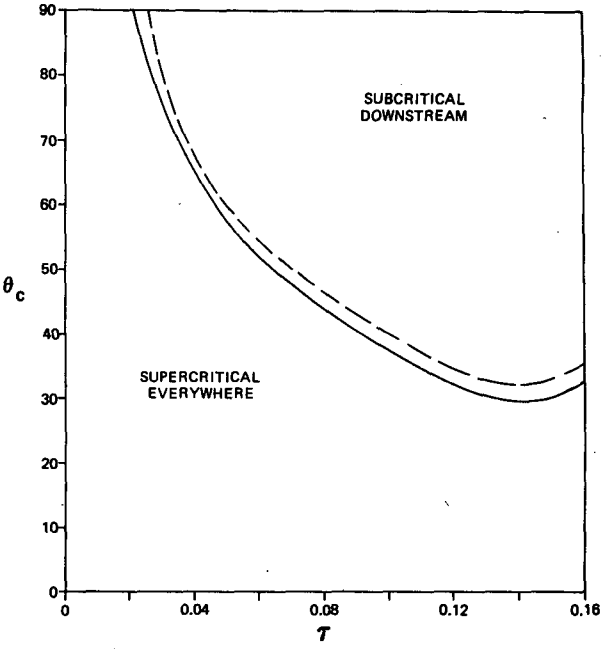

FIG. 16. Division of τ, θ_c parameter space into uniformly supercritical and downstream subcritical plume coastal currents.

Two theoretical linear stability analyses are indirectly relevant to these meanders. Paldor (1983) used a reduced gravity model of a wall-bounded buoyant current having uniform potential vorticity, no friction, and a boundary front of degenerate type. Small perturbations of all wavelength were stable. Killworth and Stern (1982) studied a similar model but with small potential vorticity gradient across the current. They found unstable long-wave fluctuations provided the potential vorticity increased toward shore and the mean current vanished at the shore. Here, in contrast, the meanders are unstable but the potential vorticity increases strongly toward offshore, the current is supercritical everywhere, and the meanders have short wavelength.

Two laboratory studies of coastal current instability

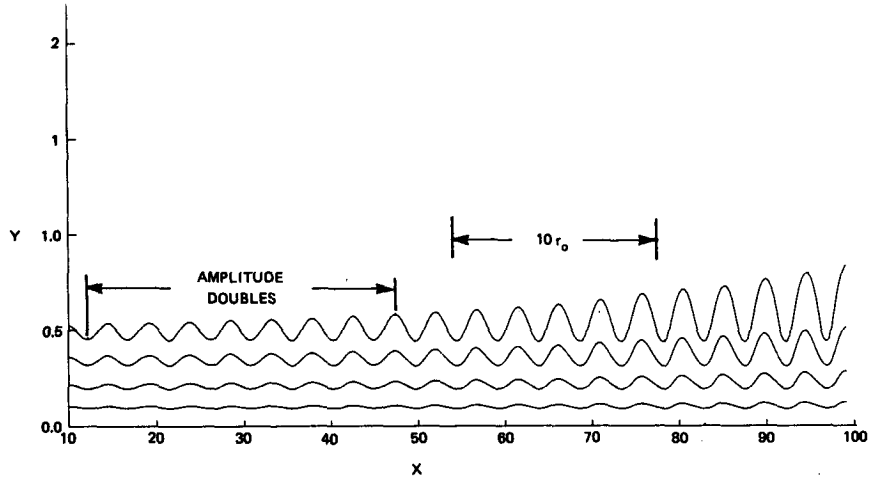

FIG. 17. Innermost four streamline shapes for the standard case in the coastal current far downstream showing meander growth.

relate to the present results. McClimans (1986) studied the dynamics of a coastal current produced in a rotating basin by discharging a light water layer upstream along a straight boundary simulating a coast. Subcritical source flows produced large anticyclonic eddies downstream which transported nearly the entire coastal current offshore. Supercritical source flows produced growing waves similar to the present results which ultimately broke at the crests downstream. Griffiths and Linden (1981) observed the growth of waves on the upper layer of lighter fluid above heavier fluid in a rotating annulus. After the fluid in the annulus had achieved uniform rotation, the outer annulus wall was withdrawn. The upper layer then adjusted from uniform depth and no current to a quasi-geostrophic coastal current with a boundary front at the outer edge. Apart from friction and mixing effects, the flow had uniform potential vorticity. Amplifying waves formed on this current for all flow conditions, ultimately producing dipole vortices along the front. The experiment with greatest correspondence to the present results had a relatively thin upper layer ($d_0/h \approx 0.3$), $F > 1$ everywhere, and an initial upper layer width of about $0.4r_0$. The linear analysis for baroclinic (two coupled layers) instability applied to this flow predicted baroclinic stability. Thus, they interpreted the unstable waves for this and related flows as likely the action of barotropic (one layer) instability, as in the present results. (Presumably the friction and mixing produced sufficient gradient in potential vorticity to permit instability and render Paldor's (1983) results inapplicable.) Their wave properties are best compared with those for separation here ($\tau = \tau_s = 0.16$). They found a mean current width of $1.0r_0$, compared to $0.75r_0$ here, and wavelength of $\lambda \approx 3r_0$, compared to $2.3r_0$ here. The relative closeness of these properties argues that quite similar dynamics is active, despite the very different methods of wave production in the two studies.

TABLE 1. Coastal current meander properties.

τ	K	θ_c	λ/w	λ/r_0	x_2/w	x_2/r_0
0.02	0.090	90°	14.6	1.3	73.5	6.6
0.10	0.432	40°	4.7	2.0	48.0	20.7
0.16	0.683	30°	3.3	2.3	37.2	25.4

8. Concluding remarks

I have developed a layer model that includes fronts as discontinuities to study the steady state behavior of estuary plumes on the continental shelf where the plume depth is a small fraction of the total water depth. The complete range from small-scale, nonrotating to large-scale, rotating plumes was included. The two length scales of the flow are the outlet channel width w and the baroclinic Rossby radius r_0; their ratio forms the Kelvin number K with $K = 0$ representing the nonrotating or small-scale plume limit. I used Gill's (1977) model of rotating channel flow to formulate the upstream flow state in the outlet channel. I assumed, following G82, supercritical flow in the outlet channel at the estuary mouth and used the method of characteristics to compute the flow state, including fronts, downstream.

In the nonrotating limit, $K = 0$, the model plume structure is dominated by a strong boundary front, called a discharge front, which serves as the offshore plume boundary. Because of its relatively great strength, as indexed by the large value of the plume layer depth behind it, considerable downward entrainment occurs there so that appreciable buoyant water is lost to the plume by local vertical mixing with ambient water.

These plumes reach their greatest depths offshore at the discharge front because only cross-stream pressure gradient is available to turn the plume water toward alongshore, Coriolis force being absent. Especially in the concentration of isopycnal depth and mass transport offshore near the front, small-scale plumes are distinct from large-scale ones. At large outlet channel angles this concentration ultimately forms a ring structure quite similar to that found in time-dependent, radially symmetric plumes released from a small source. At these larger angles the right-hand channel streamline separates from the shore, leaving ambient water between it and the coast at the surface.

Admission of rotation, even a relatively modest amount, introduces the additional length scale of the Rossby radius r_0, and with it much richer structure and dynamics. The plume streamlines turn anticyclonically after discharge because of Coriolis action and move toward shore. This turning region is dominated by nearly inertial momentum balance and so has strongly nonlinear dynamics. The discharge front weakens and becomes degenerate with corresponding high levels behind it of shear Froude number; consequently, the resultant local vertical mixing would likely render it unobservable. For the larger outlet channel angles the innermost streamline separates from the shore, as in the nonrotating limit. Nevertheless, this streamline now also bends back to shore and reattaches to the coast, leaving an isolated body of ambient water at the surface upstream. As the plume streamlines near the coast they are turned cyclonically to form a nearly geostrophic coastal current. Near the estuary mouth this turning is gradual and the coastal current weak, but as more streamlines arrive near shore another front forms, an interior front that I call the coastal front because it bounds the developing coastal current. This front strengthens as the coastal current builds behind it. As plume water crosses it, intense local dissipation reduces its total energy, while the streamlines turn abruptly toward alongshore, the cross-stream momentum balance switches to nearly geostrophic, and the potential vorticity amplifies, producing a large cross-stream gradient of potential vorticity in the coastal current. Further downstream the coastal front weakens and becomes degenerate while meanders develop in the coastal current of short wavelength, about two Rossby radii. These meanders are unstable, growing slowly downstream to double their amplitude after about $20r_0$. While no mathematical models of which I am aware address such coastal current instability, quite similar unstable short waves were produced by Griffiths and Linden (1981) in their laboratory study.

The model results show that low Kelvin numbers or low outlet channel angles or both result in plumes that remain supercritical everywhere, while high Kelvin numbers and outlet angles result in subcritical flow downstream in the coastal current, despite the initial supercritical channel state. In the latter case flow conditions downstream will propagate upstream to where the Froude number first reaches unity.

The model reveals interesting behavior by the discharge front. Without rotation it remains of the depth discontinuity type while slowly losing strength downstream. With rotation it begins as a depth discontinuity type, but subsequently undergoes transition to the degenerate type where no important local frontal dynamics is present, merely a free streamline. Most geophysical models that use a layer formulation assume that all boundary fronts are of the degenerate type, but here the transition from one type to the other is highlighted.

The model plume dynamics is remote from any linear model formulation. The supercritical flows and nondegenerate fronts in such flows present formidable challenges to construction of an analytic model. Not only does the momentum balance itself frequently demand inclusion of the nonlinear acceleration terms, but the discontinuous switching across the coastal front of the momentum balance from nearly inertial to nearly geostrophic has strong nonlinear character.

An abundance of analogous structure to that found here may be found in the large body of literature on compressible gas flows. Figure 18, adapted from Liepmann and Roshko (1957), shows the formation of a shock wave in steady, supersonic flow along a wall that makes a gradual turn inward through angle θ. This flow is directly analogous to the plume flow here in its coastal front formation. The supersonic upstream flow in Fig. 18 is analogous to that of the plume approaching the coast at supercritical speeds in Fig. 7, while the downstream flow, turned left through angle θ in Fig.

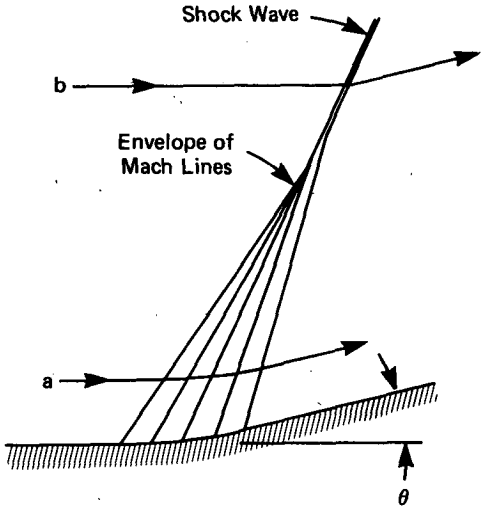

FIG. 18. Analog in compressible gas flow to coastal front formation (Fig. 7). A supersonic, steady flow encounters a bend in a wall, forcing a total streamline angle change of θ. Streamline marked "a" traverses region of Mach lines (characteristic lines) radiating from wall at curve and gradually turns through angle θ. Streamline marked "b" traverses the shock wave, analogous to the coastal front, and turns abruptly. After Liepmann and Roshko (1957, Fig. 4.7).

18, is analogous to that in Fig. 7 which has turned left to parallel the coast. Left-running characteristic lines, called Mach lines, radiate from the wall in Fig. 18 signaling through pressure changes across them the kinematic requirement for leftward streamline turning. These lines coalesce to form a shock wave. Streamlines turn gradually left in traversing the region below the shock but abruptly left across the shock. Across the shock flow properties change discontinuously, that is, on a different scale, including density and vorticity, analogous to layer depth and potential vorticity in the shallow water model. In the frictionless region behind the shock the gradient of vorticity across streamlines is given by Crocco's vorticity theorem (Crocco, 1937; Tsien, 1958), analogous to (4b) here. We may anticipate, then, that much useful guidance for solving other, similar geophysical flows to the present one may also be available in the well-established gas dynamics literature.

Acknowledgments. This work was supported by funds from the National Science Foundation, Physical Oceanography Program through Grant OCE-8315207. The School of Ocean Sciences, University College of North Wales at Bangor, U.K., through the initiative of Prof. John H. Simpson, kindly provided computing resources and helpful discussions of the work during my sabbatical leave there.

APPENDIX

Solution Method for Degenerate Fronts

Plumes with rotation or finite K have boundary fronts that become degenerate downstream: either the discharge front, the coastal front, or both. By definition, a degenerate front is one where the layer depth D and phase speed C vanish behind the front on the horizontal scale of the plume, not on the frontal scale associated with depth discontinuity fronts for which $D_f > 0$. Consequently, at a degenerate front the method of characteristics becomes unusable, because no characteristic line can intersect the front as C, and therefore ϕ in (5a), vanishes. Furthermore, the jump conditions (7) become meaningless, because there is no jump. The front, instead, is a mere free streamline.

To find the flow properties at a degenerate front and the front's trajectory one must combine its known properties with (12a), the cross-stream momentum equation. The known properties are

$$D_f = 0 = C_f,$$

$$\Psi = \Psi_f = \text{const},$$

$$B = B_f(\Psi_f) = \text{const} = D_f + \frac{Q_f^2}{2}.$$

Thus, $Q_f = (2B_f)^{1/2} = \text{const}$.

The remaining flow variables are the frontal angle α and streamline angle θ_f; however, since the front is a streamline, $\alpha(X) = \theta_f(X)$. One may then utilize (12a), transformed to X, Y from S, N variables, to find

$$\frac{d\theta_f}{dX} = -\frac{K}{U_f} - \frac{1}{U_f^2}\left(\frac{\partial D}{\partial Y}\right)_f, \tag{A1}$$

where

$$U_f = Q_f \cos\theta_f.$$

When the criterion $D_f < 10^{-6}$ was first satisfied in marching downstream at X, I began implementing this method. I computed $Y_f(X + \Delta X) = Y_f(X) + \tan\theta_f(X)\Delta X$ and solved for the flow field at $X + \Delta X$ for all interior points $Y < Y_f(X + \Delta X)$ at uniform intervals ΔY using the method of characteristics. Then I computed the layer-depth slope $(\partial D/\partial Y)_f$ from the form

$$D(Y) = (Y_f - Y)[a_0 + a_1(Y_f - Y)]. \tag{A2}$$

Here a_0 and a_1 were constants found by imposing a least-squares fit through the five nearest interior points in Y where D was known. This form had the advantage of coupling both the frontal position Y_f and the interior layer depth field to the computation of slope. From (A2) one has $(\partial D/\partial Y)_f = -a_0$. I then used (A1) to compute $d\theta_f/dX$, and thus found $\theta_f(X + \Delta X)$. The same cycle was then repeated downstream.

At the degenerate fronts formed by streamlines that had separated from the shoreline, as for the streamline in Fig. 15 labeled "$D = 0$", a_0 was zero in (A2) so that the pressure gradient term in (A1) vanished, the momentum balance was inertial, and $d\theta_f/dX$ corresponded to motion along an inertia circle. At boundary fronts, however, both terms on the right of (A1) were generally important. As the discharge front became degenerate, a_0 became small and the flow became nearly inertial, but after the coastal front became the boundary front downstream and subsequently weakened to become degenerate, the pressure gradient term fluctuated in the meander region. At meander crests the front was most extended, the plume thinnest, and so $(\partial D/\partial Y)_f$ had a least negative value; consequently, the Coriolis term was ascendant and $d\theta_f/dX$ negative. The reverse was true at meander troughs, so that $d\theta_f/dX$ was positive there. Thus, the degenerate front participated in the oscillations of the meander region.

REFERENCES

Beardsley, R. C., and J. Hart, 1978: A simple theoretical model for the flow of an estuary onto a continental shelf. *J. Geophys. Res.*, **83**, 873–883.

Boicourt, W. C., 1973: The circulation on the continental shelf from Chesapeake Bay to Cape Hatteras. Ph.D. dissertation, The Johns Hopkins University.

Chao, S.-Y., and W. C. Boicourt, 1986: Onset of estuarine plumes. *J. Phys. Oceanogr.*, **16**, in press.

Charney, J., 1955: The Gulf Stream as an inertial boundary layer. *Proc. Natl. Acad. Sci.*, **41**, 731–740.

Courant, R., and K. O. Friedrichs, 1976: *Supersonic Flow and Shock Waves*. Interscience, 464 pp.

Crocco, L., 1937: Eine neue Stromfunktion für die Erforschung der

Bewegung der Gase mit Rotation. *Z. Angew. Math. U. Mech.*, **17**, 1–7.

Garvine, R. W., 1974a: Physical features of the Connecticut River outflow during high discharge. *J. Geophys. Res.*, **79**, 831–846.

——, 1974b: Dynamics of small-scale oceanic fronts. *J. Phys. Oceanogr.*, **4**, 557–569.

——, 1977: Observations of the motion field of the Connecticut River plume. *J. Geophys. Res.*, **83**, 441–454.

——, 1981: Frontal jump conditions for models of shallow, buoyant surface layer hydrodynamics. *Tellus*, **33**, 301–312.

——, 1982: A steady state model for buoyant surface plume hydrodynamics in coastal waters. *Tellus*, **34**, 293–306.

——, 1984: Radial spreading of buoyant, surface plumes in coastal waters. *J. Geophys. Res.*, **89**, 1989–1996.

——, and J. D. Monk, 1974: Frontal structure of a river plume. *J. Phys. Oceanogr.*, **16**, 2251–2259.

Gill, A. E., 1977: The hydraulics of rotating-channel flow. *J. Fluid Mech.*, **80**, 641–671.

——, 1982: *Atmosphere-Ocean Dynamics.* Academic Press, 662 pp.

Griffiths, R. W., and P. F. Linden, 1981: Laboratory experiments on fronts. *Geophys. Astrophys. Fluid Dyn.*, **19**, 159–187.

Kao, T. W., C. Park and H.-P. Pao, 1977: Buoyant surface discharge and small-scale oceanic fronts: A numerical study. *J. Geophys. Res.*, **82**, 1747–1766.

Killworth, P. D., and M. E. Stern, 1982: Instabilities on density-driven boundary currents and fronts. *Geophys. Astrophys. Fluid Dyn.*, **22**, 1–28.

Liepmann, H. W., and A. Roshko, 1957: *Elements of Gasdynamics.* Wiley & Sons, 439 pp.

McClimans, T. A., 1986: Laboratory modeling of dynamic processes in fjords and shelf waters. *The Role of Freshwater Outflow in Coastal Marine Ecosystems*, S. Skreslet, Ed., NATO ASI Series G: Ecological Science, Vol. 7, Springer-Verlag, 67–84.

Nof, D., 1978: On geostrophic adjustment in sea straits and wide estuaries: Theory and laboratory experiments. Part II—Two-layer system. *J. Phys. Oceanogr.*, **8**, 861–872.

——, 1986: Geostrophic shock waves. *J. Phys. Oceanogr.*, **16**, 886–901.

O'Donnell, J., 1986: A numerical model of the dynamics of buoyant discharges. Ph.D. dissertation, University of Delaware, 182 pp.

——, and R. W. Garvine, 1983: A time dependent, two-layer frontal model of buoyant plume dynamics. *Tellus*, **35A**, 73–80.

Paldor, N., 1983: Linear stability and stable modes of geostrophic modes. *Geophys. Astrophys. Fluid Dyn.*, **24**, 299–326.

Pratt, L. J., 1983: On inertial flow over topography. Part 1. Semi-geostrophic adjustment to an obstacle. *J. Fluid Mech.*, **131**, 195–218.

Schubel, J. R., H. H. Carter and W. B. Cronin, 1976: Effects of Agnes on the distribution of salinity along the main axis of the Bay and in contiguous shelf waters. *The Effects of Tropical Storm Agnes on the Chesapeake Bay Estuarine System.* Baltimore, The Johns Hopkins University Press, 33–65.

Simpson, J. E., 1982: Gravity currents in the laboratory, atmosphere, and ocean. *Annual Reviews in Fluid Mechanics*, Vol. 14, Annual Reviews, 213–234.

Stoker, J. J., 1957: *Water Waves.* Wiley-Interscience, 567 pp.

Takano, K., 1954: On the salinity and velocity distribution off the mouth of a river. *J. Oceanogr. Soc. Japan*, **10**, 92–98.

Tsien, H. S., 1958: The equations of gas dynamics. *Fundamentals of Gas Dynamics, Vol. III, High Speed Aerodynamics and Jet Propulsion.* H. W. Emmons, Ed., Princeton University Press, 749 pp.